ACS APPLIED MATERIALS & INTERFACES

Research Article

Cite This: ACS Appl. Mater. Interfaces 2017, 9, 43061−43071

www.acsami.org

Gas Separation through Bilayer Silica, the Thinnest Possible Silica Membrane

Bowen Yao,[†,⊥] Salvatore Mandrà,[‡,∥] John O. Curry,[†,#] Shamil Shaikhutdinov,[§] Hans-Joachim Freund,[§] and Joshua Schrier*[,†]

[†]Department of Chemistry, Haverford College, 370 Lancaster Avenue, Haverford, Pennsylvania 19041, United States

[‡]Quantum Artificial Intelligence Laboratory (QuAIL), Mail Stop 269-1, NASA Ames Research Center, Moffett Field, California 94035, United States

[∥]Stinger Ghaffarian Technologies Inc., 7701 Greenbelt Road, Suite 400, Greenbelt, Maryland 20770, United States

[§]Department of Chemical Physics, Fritz Haber Institute, Faradayweg 4-6, Berlin 14195, Germany

Supporting Information

ABSTRACT: Membrane-based gas separation processes can address key challenges in energy and environment, but for many applications the permeance and selectivity of bulk membranes is insufficient for economical use. Theory and experiment indicate that permeance and selectivity can be increased by using two-dimensional materials with subnanometer pores as membranes. Motivated by experiments showing selective permeation of H_2/CO mixtures through amorphous silica bilayers, here we perform a theoretical study of gas separation through silica bilayers. Using density functional theory calculations, we obtain geometries of crystalline free-standing silica bilayers (comprised of six-membered rings), as well as the seven-, eight-, and nine-membered rings that are observed in glassy silica bilayers, which arise due to Stone−Wales defects and vacancies. We then compute the potential energy barriers for gas passage through these various pore types for He, Ne, Ar, Kr, H_2, N_2, CO, and CO_2 gases, and use the data to assess their capability for selective gas separation. Our calculations indicate that crystalline bilayer silica, which is less than a nanometer thick, can be a high-selectivity and high-permeance membrane material for ^{3}He/^{4}He, He/natural gas, and H_2/CO separations.

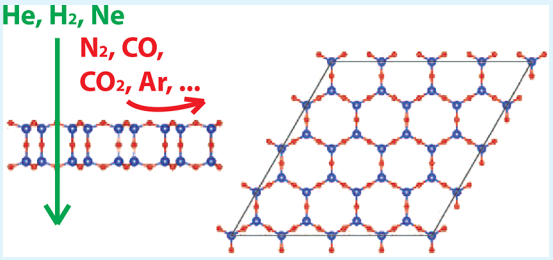

KEYWORDS: *bilayer silica, amorphous, vitreous, density functional theory, potential energy surface, resonant tunneling*

1. INTRODUCTION

Gas mixture separation is essential to many chemical manufacturing, energy generation, and environmental remediation processes. Some important separations include purification of He from natural gas (primarily CH_4),[1] H_2/CO separations for hydrogen fuel production and certain fuel cell applications,[2] and CO_2/N_2 separations for postcombustion greenhouse gas capture.[3,4] In theory, membrane processes for gas separation require less energy than alternative technologies such as pressure swing absorption and cryogenic distillation.[5−8] A wide variety of membrane materials, including metallic alloys, modified silica, zeolites, carbon molecular sieves, and polymers, have been developed for He, H_2, and CO_2 separations,[2,3,5−8] as summarized in recent reviews.[9−11] However, the economic viability could be improved by developing new membrane materials with larger permeance, selectivity, and long-term chemical stability.[5,12,13]

An emerging area in gas separation membranes is the use of two-dimensional materials, such as graphene and graphene-like two-dimensional polymers. This is the topic of several recent reviews.[14−18] Although pristine graphene is impermeable to gases,[19−21] theoretical calculations indicate that selective gas separations with high permeance can occur in sufficiently large Stone−Wales defects,[20] or subnanometer multiatom vacancies.[22] Experimental strategies such as ultraviolet - oxidative etching,[23] oxygen plasma irradiation,[24] carbothermal reactions with metal nanoparticles,[25] nanohorn-type features in graphene,[26] and even utilization of naturally occurring defects and tears in multilayer stacks of graphene[27] have been demonstrated as strategies for introducing gas-selective defects in graphene. More generally, gas separation has been also been studied for the intrinsic pores that occur in the structures of other two-dimensional materials, including other two-dimensional carbon allotropes such as graphdiyne,[28,29] two-dimensional covalent organic frameworks/polymers,[30−35] and non-carbon-based 2D materials,[16] such as silicene (the silicon analogue of graphene),[36] boron-nitride analogues of graphenylene,[37] graphitic carbon-nitride,[38] and two-dimensional metal organic frameworks (MOFs).[39] To a first approximation, the high permeance and selectivity are due to the combination of a reduced transport distance (by using an atomically thin membrane) and size-exclusion separation of the gases (by

Received: September 4, 2017
Accepted: November 20, 2017
Published: November 20, 2017

DOI: 10.1021/acsami.7b13302
ACS Appl. Mater. Interfaces 2017, 9, 43061−43071

using subnanometer pores), both of which are known from the study of bulk membranes. However, nanostructured materials have high membrane selectivity in part due to new phenomena such as quantum mechanical tunneling,[31,40−43] (classical) surface adsorption and diffusion effects,[33,44,45] and size-dependent entropic barriers.[35]

In this Article, we examine a new type of two-dimensional material, "silicatene", comprised of corner-shared tetrahedral SiO_4 building units.[46] Monolayer silica forms chemical bonds to the underlying metal support surface upon which it is grown, preventing isolation of individual, free-standing layers as is done with graphene and other nanomaterials.[47] In contrast, bilayer silica forms covalent bonds between the two layers, and thus is only weakly physisorbed to the underlying metal surface.[48−50] An illustration of the bilayer silica structure is shown in Figure 1a,b. Very recently, millimeter-scale exfoliation and transfer of silica bilayers has been demonstrated experimentally,[51,52] allowing for the possibility of using unsupported, free-standing layers. Bilayer silica exists in both crystalline (perfectly ordered) and amorphous (glassy) states in the *xy* plane, while still maintaining crystalline order in the *z*-axis. The crystalline form depicted in Figure 1a,b is comprised entirely of six-membered rings (with a structure analogous to graphene), and the amorphous form consists of a mixture of four-, five-, six-, seven-, eight-, and nine-membered rings.[53,54] Covalent bonding between the "top" and "bottom" silica layers results in a fixed alignment of positions of these rings on both sides of bilayer, as illustrated in Figure 1. The crystalline and amorphous forms coexist and can form coherent interfaces.[55] Temperature-programmed desorption experiments by Emmez et al. demonstrated that molecular deuterium (D_2) and carbon monoxide (CO) permeate through the amorphous bilayer silica, which can be attributed to passage through the naturally occurring defects, but not through crystalline bilayer silica.[56] This experiment demonstrates that some defects are sufficiently large to allow for gas transport, although it did not provide an atomistic understanding of which defects are permeable to which gases. Very little is known about this permeation process from theoretical calculations. Previous work has focused primarily on the potential energy barriers for metals, specifically Au and Pd atoms[57] and Li, Na, K, and Mg atoms[58] through the various types of glassy defects. In a theoretical study of the infrared spectra features of CO trapped between silica bilayers and Ru(0001) surfaces, Schlexer et al. calculated a potential energy barrier of 0.5 eV for penetration of CO through crystalline (six-membered ring) bilayer silica supported on Ru(0001).[59] Additionally, Kostinski et al. modeled the water diffusion through amorphous silica using calculations on small silica bilayer-like clusters.[60]

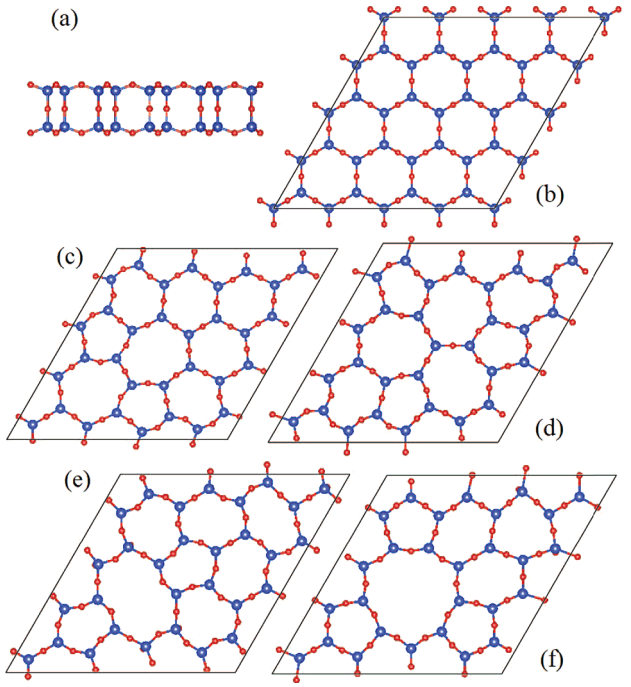

Figure 1. Silica bilayer geometries considered in this work. Red and blue indicate oxygen and silicon atoms, respectively. (a) Side view and (b) top view of the crystalline structure; (c) Stone−Wales (SW) defect; (d) divacancy 555777 defect; (e) divacancy 585 defect; and (f) tetravacancy defect.

In this Article, we characterize the gas transport through crystalline and glassy bilayer silica. Using density functional theory calculations, we obtain the geometries of crystalline bilayer silica and the Stone−Wales type defects that occur in glassy bilayer silica for unstrained, unsupported, free-standing systems. Using these geometries, we characterize the potential energy barrier for transmission of He, Ne, Ar, Kr, H_2, N_2, O_2, CO, and CO_2 gases through the various glassy defects. These results allow us to rationalize previous temperature-programmed desorption experiments[56] and determine the structural features needed for industrially important gas separation processes, specifically He/natural gas separation, H_2/CO separations for fuel cells, and N_2/CO_2 separations for greenhouse gas capture.

2. COMPUTATIONAL METHODS

Density functional theory calculations were performed using the projector-augmented wave method (PAW)[61,62] general gradient approximation Perdew−Burke−Ernzerof (GGA-PBE)[63,64] pseudopotentials, utilized in VASP version 5.3.5.[65−67] Dispersion interactions are included using Grimme's D2 model.[68,69] Schlexer et al. discussed the importance of including dispersion corrections in treating CO adsorption on silica bilayers, and found that the PBE-D2 model is comparable to other models such as optB88-vdW and HSE06+D.[59] All calculations were performed with a 5 × 5 × 1 Monkhorst−Pack grid.

Initial geometry optimizations of the structures shown in Figure 1 were performed for a force convergence of 0.005 eV/Å. Potential energy calculations were performed by putting the optimized silica bilayer into a box with a length of 20 Å perpendicular, creating a vacuum region of 15.6 Å between the periodic replicas of the silica bilayer, keeping the geometry fixed, and calculating the potential energy as the gas molecules approached. To facilitate future efforts at fitting classical molecular dynamics force-fields for the silica−gas interaction potential, the bond lengths of diatomic and triatomic gases (H_2, N_2, CO, and CO_2) were kept fixed at the values used in common force-fields for these gases, specifically H_2 at 0.7414 Å,[70] N_2 at 1.0464 Å,[71] CO at 1.1405 Å,[72] and CO_2 at 1.149 Å for the C−O distance.[73]

3. RESULTS AND DISCUSSION

3.1. Defect Geometries. Crystalline silica bilayers consist of a hexagonal lattice of corner-shared SiO_4 tetrahedra, as shown in Figure 1a,b. A 4 × 4 supercell of free-standing (i.e., not metal-supported) silica was used to allow for geometry relaxations, resulting in an optimized lattice constant of 21.189 Å for the supercell, or 5.297 Å for the primitive lattice constant. See the Supporting Information for a complete set of optimized atomic positions. This is 3% smaller than the values reported for metal-supported crystalline silica bilayers. (For example, the

DOI: 10.1021/acsami.7b13302
ACS Appl. Mater. Interfaces 2017, 9, 43061−43071

calculations of Schlexer et al. for Ru(0001)-supported crystalline bilayers used a unit cell length of 5.455 Å,[59] which is very close to the 5.42 Å expected for a crystalline film on Ru(0001) forming a (2 × 2) structure.) The discrepancy in the lattice constants is due to interactions with the metal substrate that expand the silica bilayer structure. As discussed below, because the potential energy barriers for gas transport scale roughly with the size of the various pores, a consequence of this is that the potential energy barriers for gas transport through the free-standing sheet will be systematically higher than that of metal-supported structures.

Vitreous silica bilayers exhibit a broad ring-size distribution that ranges from four- to 10-membered rings.[54,74] The defect structures minimize distortions of the SiO_4 building units, to minimize the total energy, analogous to the manner in which graphene defect structures preserve approximate sp^2 hybridization of the carbon atom building units. These types of low-energy defect structures can be modeled within a 4 × 4 supercell.[20] The elementary defect patterns are (i) the Stone−Wales defects (Figure 1c) arising from rotation of an interbuilding unit bonds and resulting in five- and seven-membered rings; (ii) the divacancy 555777 defect (Figure 1d) resulting in five- and seven-membered rings; (iii) the divacancy 585 defect (Figure 1e) resulting in five- and eight-membered rings; and (iv) the tetravacancy defect (Figure 1f) resulting in nine-membered rings. For each of these elementary defect models, the atomic positions and the supercell lattice constant were optimized to obtain the minimum total energy of the system. See the Supporting Information for a complete set of optimized atomic positions. The optimized defect supercell lattice constants are 1−3% smaller than the optimized crystalline lattice constant, with the tetravacancy defect structure having the largest deviation.

Crystalline silica bilayers have two types of oxygen atoms (depicted as red spheres in Figure 1a): surface oxygens that are above or below the plane formed by the blue silicon atoms and interior oxygens that located at the center of the sheet between the two planes of silicon atoms. The surface oxygens in crystalline silica bilayers are uniformly 2.173 Å above and below the center of the sheet. Introducing defects distorts the lattice, causing the oxygen atoms to adopt new positions that are above or below the undistorted position. Figure 2 shows the distribution of vertical displacement of the surface oxygen atoms from the geometric center of each of the defect structure models; the red-dashed line indicates the crystalline surface oxygen atom distance. The Stone−Wales defect (Figure 2a) has a roughly symmetrical effect on oxygen positions, unlike the other defect structures. These other structures arise from vacancy defects, and thus a more substantial reconstruction is required. With the exception of the 555777 divacancy defect (Figure 2b), oxygen atoms are pushed both further and closer to the center than the positions found in the crystalline sheet (indicated by the red-dashed line). The most extreme cases occur for the 585 divacancy and tetravacancy structures, in which some oxygen atoms are >0.2 Å closer to the center than the crystalline structure.

Previous studies of gas transport through graphene defects indicate that larger defects tend to have smaller potential energy barriers.[20,22,34] The effective defect size must include the finite size of the atoms, which is typically accounted for using the van der Waals radii. To quantify this property, we determined the largest radius sphere that can fit into the space created by the van der Waals radii of the silicon and oxygen atoms of each

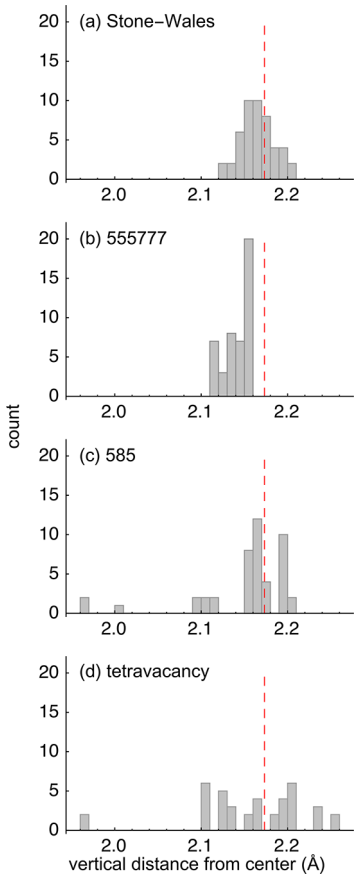

Figure 2. Distribution of oxygen positions relative to the center plane of the silica bilayer. The red-dashed line indicates the distance for the crystalline silica bilayer. (a) Stone−Wales defect; (b) 555777 divacancy; (c) 585 divacancy; and (d) tetravacancy.

structure. Table 1 shows these sphere radii in ascending order. Note that not all rings with the same number of members have

Table 1. Radius of the Largest Sphere That Fits Inside Each Pore

structure	ring size	radius[a]
585 divacancy	5	0.29
Stone−Wales defect	5	0.35
555777 divacancy	5	0.39
tetravacancy	5	0.44
crystalline	6	0.96
Stone−Wales defect	7	1.16
585 divacancy	8	1.17
555777 divacancy	7	1.28
tetravacancy	9	2.28

[a]Sphere radius in angstroms.

the same sizes. For example, the five-membered rings vary by 50% in radius, and the two different types of seven-membered rings vary by 10% in size. The pore size is generally, but not strictly, monotonic with the ring size; for example, the eight-membered ring defects in the 585 structure are smaller than the seven-membered ring defects in the 555777 structure, due to the shape of the defect. This information also provides some initial guidance on gas separation properties. For example, even the largest five-membered ring is less than one-half the size of the six-membered ring. Thus, the five-membered rings make an

DOI: 10.1021/acsami.7b13302
ACS Appl. Mater. Interfaces 2017, 9, 43061−43071

insignificant contribution to gas transport even for the smallest gases. On the other hand, the nine-membered ring is more than twice the size of the crystalline six-membered ring, and is larger than the van der Waals radius of xenon and the kinetic diameter of methane. The potential energy barrier calculations described below confirm that defects consisting of nine-membered (or larger) rings are incapable of size-selective separations of the gases considered here.

3.2. Potential Energy Barriers for Gas Permeation. Using the optimized structures described above, we next computed the potential energy for passage of He, Ne, Ar, Kr, H_2, N_2, O_2, CO, and CO_2 gases through each of the defect types, as a function of position. In all of these plots, the center of the bilayer silica is taken as zero, and the potential energy is plotted as a function of the center of the gas molecules distance from this point. With the exception of CO, all of the molecules are symmetrical, and thus only the unique portion of the potential energy is plotted.

The noble gas results shown in Figure 3 illustrate the trends of varying gas sizes and types.

Three qualitatively different types of potential energy surfaces (PES) occur, depending on the relative sizes of the gas and defect. Consider the example of helium, depicted in Figure 3a. The Type I PES (shown in black) has a potential energy minimum on the silica surface corresponding to a physisorbed gas molecule 4.0 Å from the center, a potential energy maximum as the gas enters the bilayer (here at 2.1 Å), and a potential energy minimum between the silica bilayers corresponding to a trapped gas molecule (here at 0.0 Å, i.e., the center of the silica bilayer). The potential energy barrier characteristic of the Type I PES occurs when the size of the gas molecule is larger than or comparable to the size of the pore (as reported in Table 1). For helium and neon gases (Figure 3a and b, respectively), this occurs only for passage through the crystalline six-membered ring. For the larger argon atom (Figure 3c), this type of repulsive barrier also occurs for all of the seven- and eight-membered ring defects.

Like the Type I PES, the Type II PES (shown in red) consists of two local minima (one on the exterior surface and one inside the bilayer) and a local maximum. The difference is that the local maximum has an attractive (negative) potential energy as compared to the noninteracting gas−silica system. Thus, the Type II PES has no barrier for ballistic gas transport (because the entering gas molecule will have a positive kinetic energy), but does have an effective barrier for gases attempting to enter the pore after being physisorbed on the surface. A Type II PES occurs when the pore is slightly larger than the gas molecule, which occurs for helium and neon with all of the seven- and eight-membered ring defects, but never for argon or larger gases. The exact position of the physisorption local minimum outside the bilayer varies from 3.2−3.7 Å, depending on the defect type. Both Type I and Type II PESs have stable states where the gas molecule is within the bilayer. For He and Ne (Figure 3a,b), this interior position is energetically more stable than the free gas (indicated by the horizontal gray dotted line at 0.00 eV), indicating that the interior trapped states are thermodynamically stable. Moreover, this interior position is more stable than the physisorbed surface state for He and Ne gases. For Ar transport through the crystalline six-membered ring (Figure 3c), this interior state may be kinetically trapped by the large potential energy barrier for exit, despite being significantly higher in energy than the free gas. This interior state is increasingly stabilized for the various seven- and eight-membered ring defects, due to the surrounding, attractive dispersion interactions.

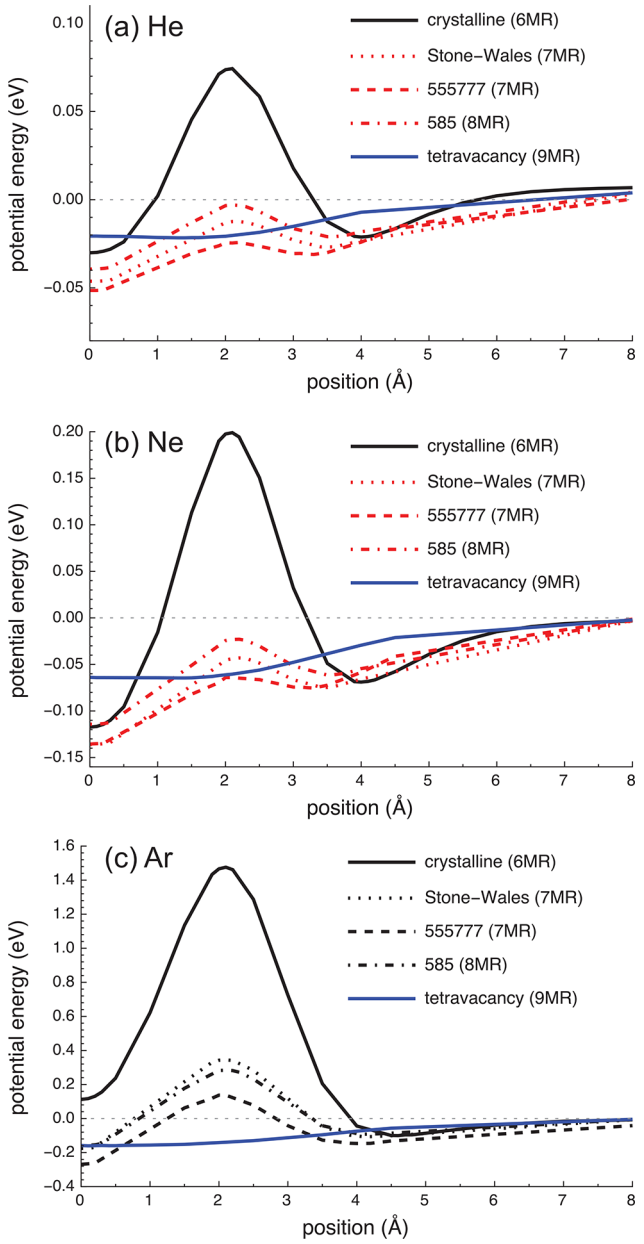

Figure 3. Potential energy for monatomic noble gases as a function of position, measured from the center of the bilayer. (a) Helium; (b) neon; and (c) argon. Black, red, and blue indicate three types of potential energy barriers described in the text.

Finally, a Type III PES (shown in blue) has no potential energy barrier, and consists of approximately only a single local energy minimum within the bilayer. In fact, He and Ne have a small (1 meV) barrier at z = 0.0 Å, which is not visible at the scale of the Figure 3, but this is absent in Ar and Kr. A Type III PES occurs when the pore is significantly larger than the gas molecule, specifically here for the nine-membered rings arising from the tetravacancy defect. Type III behavior occurs for all of the gases passing through the nine-membered ring defect, including krypton and the polyatomic gases discussed below. Although a Type III PES presents no barrier to ballistic gas transport, gases could be adsorbed in the defect, slowing their transport rate. For He and Ne, the well depth in the Type III

DOI: 10.1021/acsami.7b13302
ACS Appl. Mater. Interfaces 2017, 9, 43061−43071

PES is nearly the same as the exterior physisorption minima found in the Type I and Type II PES. Surprisingly, for the diatomic gases discussed below, the Type III minimum is 30−50 meV more stable than the exterior physisorption minimum of the corresponding Type I and Type II PES, because the linear molecules maximize its attractive dispersion interactions with the edge of the entire bilayer silica ring.

The potential energy surfaces for molecular hydrogen, nitrogen, and carbon dioxide transport through the silica bilayer are shown in Figure 4. Like the noble gases, the three types of potential energy surfaces occur depending on the relative sizes of the molecules and the ring size. The PES of the smallest molecule, H_2 (shown in Figure 4a), is qualitatively similar to that of the comparably sized helium atom (Figure 3a). The only difference is a shallow double-well potential for H_2 within the crystalline (six-membered ring) bilayer (black solid curve in Figure 4a), consisting of two local minima separated by a 5 meV barrier at the geometric center. None of the other gases we computed have this property for a Type I barrier.

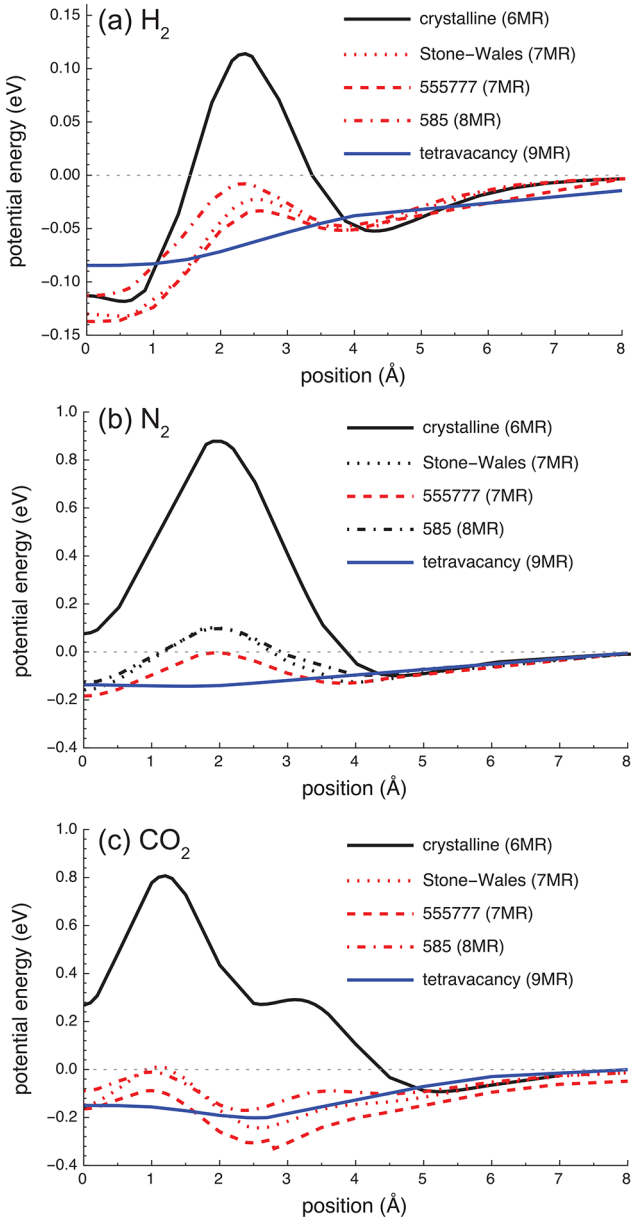

Figure 4. Potential energy for linear polyatomic gases as a function of position, measured from the center of the bilayer to the center of the molecule. (a) Hydrogen; (b) nitrogen; and (c) carbon dioxide. Black, red, and blue indicate three types of potential energy barriers described in the text.

The N_2 molecule PES (shown in Figure 4b) is qualitatively similar to that of Ar (Figure 3c). Like Ar, the local minimum at z = 0.0 Å for the crystalline six-membered ring is higher in energy than the free gas. The Stone−Wales seven-membered ring and 585 divacancy eight-membered ring potential energy surfaces overlap with one another at the scale of this plot. Finally, passage through the nine-membered ring (blue solid line) has a local minimum at 1.5 Å from the center, with a small (5 meV) barrier at the center, similar to the small double-well potential barrier observed for the H_2 molecule in the six-membered ring (Figure 4a) discussed above.

The larger triatomic CO_2 molecule (shown in Figure 4c) has additional PES features that are not seen in the monatomic and diatomic gases. First, CO_2 has a lower potential energy barrier for entry than N_2 for all of the defects. If one considers both molecules as cylinders, CO_2 has a small effective diameter than N_2, due to the electron density distribution.[33] The lower potential energy barrier for entry of CO_2 is especially pronounced for the seven- and eight-membered ring defect curves. Second, the potential energy surface has an additional local minimum and local maximum, as the end and center of the CO_2 molecule interact with distinct layers of the silica structure. Finally, for the nine-membered ring defect (solid blue line), the minima occur at 2.5 Å, and are separated by 0.052 eV at the geometric center of the bilayer. This is qualitatively similar to the Type III N_2 PES (Figure 4b), but with a larger central barrier.

Figure 5 summarizes the PES local minima (red) and maxima (black) for all of the gases as they transit through each of the pores. Within each inset, the gases are arranged in order of increasing kinetic radii. For purposes of comparison, it is useful to recall that k_BT at 298.15 K is 0.026 eV. Type I behavior corresponds to cases where the local maxima (black) have positive energies, Type II behavior to cases where the maxima (black) have negative energies, and Type III behavior to cases where there is only one minimum (single red bar) or a series of minima and maxima with very close values of energy. Figure 5a indicates that the barriers for penetrating six-membered rings for He, Ne, and H_2 are significantly lower than those of the other gases, indicating that these are the only gases that can permeate through crystalline bilayer silica with significant rate. In contrast, the barriers are smaller or nearly absent for the larger ring defects, with the exception of argon and krypton gases. (Note the change in vertical axis scale for the subsequent insets.) For the nine-membered ring defect (Figure 5e), all gases have Type III PES behavior, where the entry into the pore is barrierless and there is only a small relative potential energy barrier for transmission. The physisorption binding energies for this central position follow the expected relationship between increasing atomic/molecular polarizability and increasing attractive dispersion interactions.

To facilitate comparison of the heterodiatomic carbon monoxide to the other (symmetrical) gases, Figure 5 shows both the carbon-atom-first entry and the oxygen-atom-first entry directions, indicated as CO and OC, respectively. The external physisorbed state (rightmost red bar) is more stable for the carbon-first geometry than for the oxygen-first direction.

DOI: 10.1021/acsami.7b13302
ACS Appl. Mater. Interfaces 2017, 9, 43061−43071

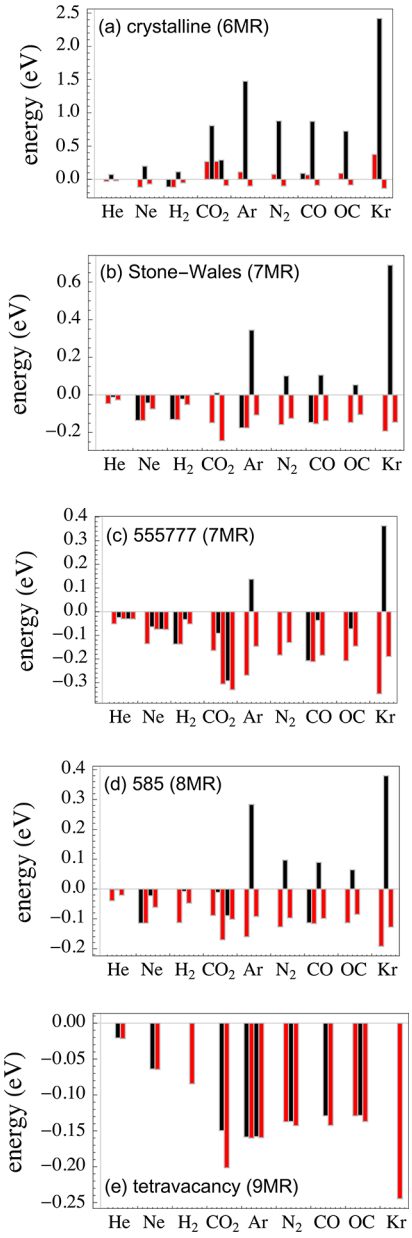

Figure 5. Summary of potential energy local minima and maxima for transmission through the silica bilayer, with gases ordered by increasing kinetic radii. Black bars indicate local maxima, and red bars indicate local minima. The left-most bar in each series indicates the value at center, and the series proceeds from the center of the silica bilayer outward. (a) Crystalline six-membered ring; (b) Stone−Wales defect seven-membered ring; (c) 555777 divacancy defect seven-membered ring; (d) 585 divacancy defect eight-membered ring; and (e) tetravacancy nine-membered ring.

The difference ranges from as little as 0.005 eV for the crystalline (Figure 5a) and tetravacancy (Figure 5e) cases, to as large as 0.039 eV for the 555777 divacancy (Figure 5c). Second, the barrier to entering the bilayer is lower for the O-first direction in all cases. In general, this difference is largest for the higher barrier cases. For example, the barrier height differences are as large as 0.147 eV for the six-membered ring, and as small as 0.025 eV for the eight-membered ring. In summary, the physisorption in the C-first direction is more energetically favorable, but entry into the bilayer in the O-first direction has a lower activation barrier.

3.3. Quantum Tunneling Effects for Helium Transmission.

Quantum tunneling effects can significantly increase the transmission of low-mass gases through two-dimensional nanoporous materials.[31,41,42] This is especially pronounced in the case of resonant tunneling through double-barrier potentials, which increases the nonclassical isotope effect.[43] The naturally occurring double barrier potential provided by crystalline bilayer silica (recall that only one-half of the potential energy surface is plotted in Figure 3) has barrier heights and interbarrier separations close to the optimal values for ^{3}He/^{4}He separation found in previous studies.[43] To examine the effect of resonant tunneling, we computed the transmission probability as a function of incident particle kinetic energy (Figure 6a) and the thermal rate constant as a

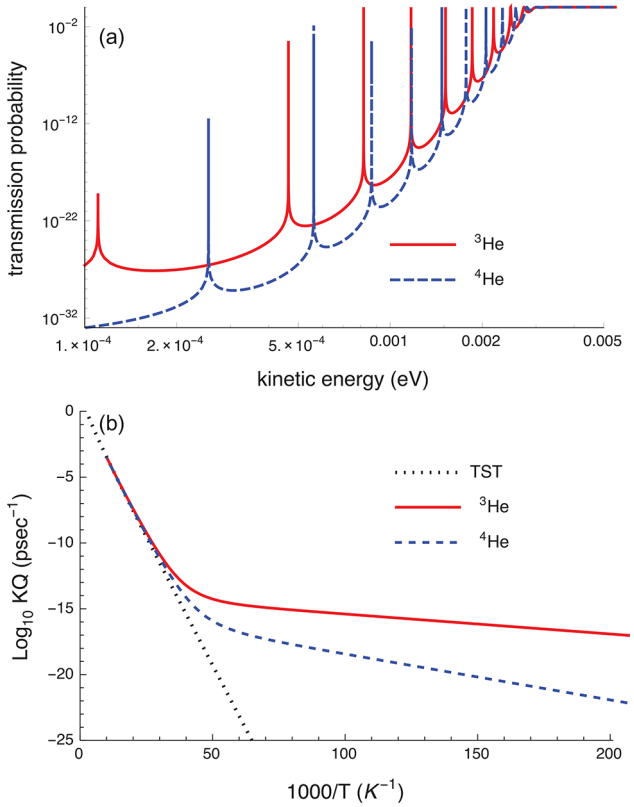

Figure 6. Resonant tunneling of ^{3}He and ^{4}He through crystalline bilayer silica. (a) Transmission as a function of incoming particle kinetic energy. (b) Thermal rate constant, as compared to transition state theory (TST).

function of temperature (Figure 6b), using the time-independent approach described in our previous work.[43,75] The potential was described by fitting three Gaussian functions to the $x \geq 0$ region shown in Figure 3a.

Each resonant transmission peak in Figure 6a corresponds to a quasibound (metastable) state of the atom inside the double-barrier potential. Approximating the region inside the barrier ($-2 \leq x \leq +2$ Å in Figure 3a) as a harmonic potential, then the eigenvalues spacing is inversely proportional to the square root of the oscillator (i.e., the helium atom) mass. By this reasoning, one expects the ^{4}He peaks occur at lower energies. However, in this case, the lowest ^{4}He transmission is missing, because the peak is narrower than machine precision. This extreme narrowness also means that this missing peak contributes insignificantly to the thermal rate constant, and

DOI: 10.1021/acsami.7b13302
ACS Appl. Mater. Interfaces 2017, 9, 43061−43071

Table 2. Energetic Span, δE, in eV

	He	Ne	H_2	CO_2	Ar	N_2	CO	Kr
crystalline (6MR)	0.104	0.316	0.232	0.900	1.576	0.977	0.962	2.554
Stone–Wales (7MR)	0.046	0.136	0.132	0.254	0.520	0.259	0.259	0.882
555777 (7MR)	0.051	0.136	0.137	0.330	0.406	0.184	0.211	0.710
585 (8MR)	0.039	0.114	0.113	0.170	0.444	0.224	0.205	0.572
tetravacancy (9MR)	0.022	0.065	0.085	0.202	0.160	0.143	0.142	0.245

Table 3. Logarithmic Selectivity, $\log_{10} S_{X/Y}$, of Crystalline Bilayer Silica for Gas Pairs at T = 300 K

	He	Ne	H_2	CO_2	Ar	N_2	CO	Kr
He		3.5	2.1	13.3	24.6	14.6	14.3	40.9
Ne	−3.5		−1.4	9.7	21.0	11.0	10.8	37.4
H_2	2.1	1.4		11.1	22.4	12.4	12.2	38.8
CO_2	−13.3	−9.7	−11.1		11.3	1.3	1.0	27.6
Ar	−24.6	−21.0	−22.4	−11.3		−10.0	−10.3	16.3
N_2	−14.6	−11.0	−12.4	−1.3	10.0		−0.3	26.3
CO	−14.3	−10.8	−12.2	−1.0	10.3	0.3		26.6
Kr	−40.9	−37.4	−38.8	−27.6	−16.3	−26.3	−26.6	

Table 4. Logarithmic Selectivity, $\log_{10} S_{X/Y}$, of Vitreous Bilayer Silica[a] for Gas Pairs at T = 300 K

	He	Ne	H_2	CO_2	Ar	N_2	CO	Kr
He		1.3	1.4	2.7	3.6	2.7	2.8	5.0
Ne	−1.3		0.0	1.3	2.2	1.3	1.5	3.7
H_2	−1.4	−0.0		1.3	2.2	1.3	1.4	3.6
CO_2	−2.7	−1.3	−1.3		0.9	0.0	0.1	2.3
Ar	−3.6	−2.2	−2.2	−0.9		−0.9	−0.8	1.4
N_2	−2.7	−1.3	−1.3	−0.0	0.9		0.1	2.3
CO	−2.8	−1.5	−1.4	−0.1	0.8	−0.1		2.2
Kr	−5.0	−3.7	−3.6	−2.3	−1.4	−2.3	−2.2	

[a]Weighted by the experimental distribution of ring types observed in ref 80.

thus can be safely ignored. The thermal rate constant, K, is evaluated by integrating the transmission probability times the Boltzmann factor, as a function of kinetic energies, and dividing by the reactant partition function, $Q(T)$. The thermal rate constants are plotted for the two isotopes in Figure 6b, and for comparison the transition-state theory (TST) value, which does not include tunneling, is shown as the dashed line. The ^{3}He transmission rate constant is several orders of magnitude greater than that of ^{4}He at low temperatures, and the rates of both isotopes asymptotically approach the TST result at higher temperatures. The isotope selectivity, that is, the ratio of the transmission rates for the two isotopes, strongly favors transmission of ^{3}He at low temperatures and converges to equal transmission of the two isotopes at higher temperatures. For example, the ratios decrease as 1088, 203, 47, 2.7, 1.05, and 1.02 as the temperature increases from T = 10, 15, 20, 30, 77, to 100 K, respectively. From these results, we conclude that crystalline bilayer silica is a promising material for low-temperature helium isotope separation.

3.4. Prospects for Gas Separation. A classical treatment of the barrier crossing process, without including any tunneling effects, suffices for modeling the transmission of heavier gases. From these results, we will estimate the relative permeances of the different defect types, and the selectivity of these defects for the different types of gas molecules. The potential energy minima and maxima summarized in Figure 5 can be used to compute the barrier crossing rates by applying transition state theory. As discussed earlier, the transmission process consists of several intermediates and transition states. These multistep processes can be formally described in terms of the energetic span, δE, which is the largest energy difference between an intermediate (local minimum) and any subsequent transition state (local maximum) during the barrier crossing process.[76] The energetic span serves as an apparent activation energy of the process, and thus a smaller energetic span leads to a faster reaction. Table 2 shows the computed energetic span values for the gases transiting through the various silica bilayer defects.

The selectivity for two gases, X and Y, is the ratio of the transport rates, r_X and r_Y, respectively, each of which in turn can be expressed in terms of the Arrhenius rate equation:

$$S_{X/Y} = \frac{r_X}{r_Y} = \frac{A_X\, e^{-\delta E_X/k_B T}}{A_Y\, e^{-\delta E_Y/k_B T}} \quad (1)$$

where A is the pre-exponential factor, k_B is the Boltzmann constant, and T is the absolute temperature. For simplicity, we assume the pre-exponential terms, A, are identical for all gases, as in previous work.[32,77] This assumption corresponds to neglecting the role of entropic contributions that favor transport of smaller, more spherical gas molecules (having more possible degrees of translational and rotational degrees of freedom as they enter the channel) and penalize transport of larger, more elongated gas molecules (having fewer possible degrees of freedom in the channel).[78] Thus, this assumption results in a conservative underestimate of the selectivity for separating smaller gas molecules from larger gas molecules. The selectivity of crystalline bilayer silica for the various gas pairs is shown in Table 3.

DOI: 10.1021/acsami.7b13302
ACS Appl. Mater. Interfaces 2017, 9, 43061−43071

The data contained in Table 3 allow us to evaluate the suitability of crystalline silica bilayer materials for industrial gas separation applications. (Note the logarithmic scale used in Tables 3 and 4.) For comparison, the best classical membranes have selectivities of $S_{X/Y} = 10^3$ (e.g., Nanosil templates for H_2/CO_2 separation[79]), and in many applications lower values are sufficient (e.g., $S_{X/Y} > 40$ is sufficient for postcombustion CO_2/N_2 separations[3]). Using these criteria, we can address the various industrial separations described in the Introduction. Because the kinetic diameter of Ar is less than that of methane, the He/Ar ratio provides a lower bound on the selectivity for He/natural gas separations. From Table 3 it is clear that crystalline silica bilayers greatly exceed the needs for this separation. For comparison, the best existing materials[9] have He/N_2 and He/CH_4 selectivities of approximately 10^3, which is 10−20 orders of magnitude lower than the selectivities shown in Table 3. Likewise, this material serves as an extraordinarily selective separation membrane for H_2/CO separations, far exceeding the selectivity of the best classical membrane by 9 orders of magnitude. (CVD grown silica membranes are the most selective, with $S_{X/Y} \approx 10^3$.[2]) The estimated selectivity for CO_2/N_2 separations is too low ($S_{X/Y} = 20$) to be useful.[3] However, we note that the stronger surface adsorption of CO_2 can lead to enhanced selectivity of two-dimensional membranes,[33] and future molecular dynamics simulations could resolve this question.

We can obtain a similar estimate of the selectivity of vitreous bilayer silica, by weighting the selectivities by the transmission of each ring type by the probabilities, p_i, at which each ring type is observed in experimental samples.[80] This weighted selectivity is given by

$$S_{X/Y} = \frac{\sum_i p_i \, e^{-\delta E_{X,i}/k_B T}}{\sum_j p_j \, e^{-\delta E_{Y,j}/k_B T}} \quad (2)$$

For simplicity, we assume that the four- and five-membered rings are impermeable, and that the two different types of seven-membered rings considered here occur equally in experiment. The calculated selectivities for the vitreous bilayer shown in Table 4 are all much lower than the crystalline case, due to the smaller or absent potential energy barriers for the larger ring defects. As a result, transport through the larger, nonselective defects dominates, resulting in reduced selectivity. Neither the He/Ar nor the H_2/CO selectivities for the vitreous material are sufficiently high to be useful for industrial processes. Thus, we conclude that only crystalline bilayer silica is useful for these gas separation problems.

Membrane performance also depends on the permeance. We can estimate this by using the kinetic theory of gases colliding with a surface, which follows from the Maxwell−Boltzmann distribution, as described in previous work,[31,32,77] using the δE values from Table 2. To estimate the allowed cross-section for successful reactions, we make the simple geometric assumption that only collisions within the largest radius of the largest circumscribed sphere (from Table 1) are transmitted. In the case of crystalline bilayer silica, this implies that only 12% of incident collisions that have sufficient kinetic energy are geometrically allowed to be transmitted. This approximation does not take into account the nominal kinetic radii or orientational effects on the transmission probability. Thus, while it is reasonable for helium, it systematically overestimates the transmission of larger gases. The results of these calculations, for each of the gases as a function of temperature, are shown in Figure 7. The shaded area in each set indicates the industrial acceptable permeance exceeding 10^{-10} mol m^{-2} s^{-1} Pa^{-1}. For comparison, the best existing modified CVD silica membranes used for hydrogen separation only reach this threshold at 873 K, and polymeric membranes only reach this threshold at the expense of reduced selectivity.[2] Similarly, the best existing material for helium separation, hollow fiber microporous silica membranes, has a permeance of 10^{-6} mol m^{-2} s^{-1} Pa^{-1}.[9,81]

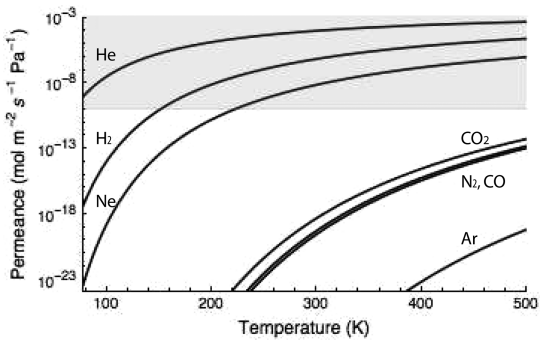

Figure 7. Computed gas permeances for crystalline bilayer silica. The shaded area indicates the industrially acceptable permeance exceeding 10^{-10} mol m^{-2} s^{-1} Pa^{-1}. The N_2 and CO curves are indistinguishable at this scale, and appear as a bold line in this plot.

From Figure 7, it is clear that only He, Ne, and H_2 are above this threshold; the other gases are many orders of magnitude too slow. The He permeance exceeds this threshold over the entire temperature range shown in Figure 7, whereas H_2 and Ne only exceed this criterion at temperatures above 145 and 216 K, respectively. Thus, at typical industrial temperatures, the permeances of these gases are sufficiently high to be of industrial value.

4. CONCLUSION

Bilayer silica is the thinnest possible stable structure for a silica membrane; if one includes the van der Waals radii of the surface oxygen atoms (1.52 Å), it is only 7.2 Å thick. We determined the geometries of the fundamental five-, six-, seven-, eight-, and nine-membered ring structures present in crystalline and vitreous free-standing two-dimensional bilayer silica. We computed potential energy barriers for the transmission of He, Ne, Ar, Kr, H_2, N_2, CO, and CO_2 gases through the optimized ring geometries. Local minima at the center of the bilayer exist for all defect types, indicating that these gases can be kinetically trapped during the transport process. In the case of the smallest gases, He, Ne, and H_2, this interior position is energetically more stable than physisorption on the surface for crystalline six-membered ring structures. Nine-membered ring structures have no potential energy barrier for any of the gases considered here, indicating that these larger defects cannot be used for selective separation. The bilayer structure serves as a double barrier potential, and quantum transmission calculations indicate that this can be used for resonant-tunneling-based separation of helium isotopes. Classical transport calculations for the other gases indicate that only crystalline bilayer silica has sufficiently high permeances and selectivities to be used for industrial He/natural gas and H_2/CO separations. In contrast, the vitreous layers increase the permeabilities of all species, and thus do not have sufficiently high selectivity for these separations. In contrast to graphene-like membranes, there is no need to

DOI: 10.1021/acsami.7b13302
ACS Appl. Mater. Interfaces 2017, 9, 43061−43071

introduce carefully designed defects to enable selective gas separation, because the crystalline silica bilayer intrinsically has the correct pore size for these separations, and the covalent bonding between the two layers enforces alignment of the pores. Our calculations indicate that the selectivity and permeance of crystalline bilayer silica exceed that of existing He and H_2 separation membrane materials by many orders of magnitude. Thus, bilayer silica is both the thinnest and the best silica membrane, and deserves further experimental investigation.

■ ASSOCIATED CONTENT

Supporting Information

The Supporting Information is available free of charge on the ACS Publications website at DOI: 10.1021/acsami.7b13302.

Optimized geometries of the structures shown in Figure 1 (PDF)

Optimized geometries of the structures shown in Figure 1, as VASP input files (ZIP)

■ AUTHOR INFORMATION

Corresponding Author

*E-mail: jschrier@haverford.edu.

ORCID

Shamil Shaikhutdinov: 0000-0001-9612-9949

Hans-Joachim Freund: 0000-0001-5188-852X

Joshua Schrier: 0000-0002-2071-1657

Present Addresses

[⊥]Department of Chemistry, University of Pennsylvania, 231 South 34th Street, Philadelphia, Pennsylvania 19104, United States.

[#]School of Law, University of Washington, 4293 Memorial Way Northeast, Seattle, Washington 98195, United States.

Notes

The authors declare no competing financial interest.

■ ACKNOWLEDGMENTS

S.M. was supported by NASA Ames Research Center. J.S. acknowledges support from the Henry Dreyfus Teacher-Scholar Award and Fulbright Foreign Scholarship. This research used resources of the National Energy Research Scientific Computing Center, a DOE Office of Science User Facility supported by the Office of Science of the U.S. Department of Energy under contract no. DE-AC02-05CH11231.

■ REFERENCES

(1) Nuttall, W. J.; Clarke, R. H.; Glowacki, B. A. Resources: Stop squandering helium. *Nature* **2012**, *485*, 573−575.

(2) Ockwig, N. W.; Nenoff, T. M. Membranes for Hydrogen Separation. *Chem. Rev.* **2007**, *107*, 4078−4110.

(3) Merkel, T. C.; Lin, H.; Wei, X.; Baker, R. Power plant post-combustion carbon dioxide capture: An opportunity for membranes. *J. Membr. Sci.* **2010**, *359*, 126−139.

(4) Boot-Handford, M. E.; Abanades, J. C.; Anthony, E. J.; Blunt, M. J.; Brandani, S.; Dowell, N. M.; Fernández, J. R.; Ferrari, M.-C.; Gross, R.; Hallett, J. P.; Haszeldine, R. S.; Heptonstall, P.; Lyngfelt, A.; Makuch, Z.; Mangano, E.; Porter, R. T. J.; Pourkashanian, M.; Rochelle, G. T.; Shah, N.; Yao, J. G.; Fennell, P. S. Carbon capture and storage update. *Energy Environ. Sci.* **2013**, *7*, 130.

(5) Bernardo, P.; Drioli, E.; Golemme, G. Membrane Gas Separation: A Review/State of the Art. *Ind. Eng. Chem. Res.* **2009**, *48*, 4638−4663.

(6) Zhao, L.; Riensche, E.; Blum, L.; Stolten, D. How gas separation membrane competes with chemical absorption in postcombustion capture. *Energy Procedia* **2011**, *4*, 629−636.

(7) Buonomenna, M. G. Membrane processes for a sustainable industrial growth. *RSC Adv.* **2013**, *3*, 5694.

(8) Baker, R. W.; Low, B. T. Gas Separation Membrane Materials: A Perspective. *Macromolecules* **2014**, *47*, 6999−7013.

(9) Scholes, C. A.; Ghosh, U. K. Review of Membranes for Helium Separation and Purification. *Membranes* **2017**, *7*, 9.

(10) Cardoso, S. P.; Azenha, I. S.; Lin, Z.; Portugal, I.; Rodrigues, A. E.; Silva, C. M. Inorganic membranes for hydrogren separation. *Sep. Purif. Rev.* **2017**, 1 DOI: 10.1080/15422119.2017.1383917.

(11) Galizia, M.; Chi, W. S.; Smith, Z. P.; Merkel, T. C.; Baker, R. W.; Freeman, B. D. 50th Anniversary Perspective: Polymers and Mixed Matrix Membranes for Gas and Vapor Separation: A Review and Prospective Opportunities. *Macromolecules* **2017**, *50*, 7809−7843.

(12) Ramasubramanian, K.; Verweij, H.; Ho, W. W. Membrane processes for carbon capture from coal-fired power plant flue gas: A modeling and cost study. *J. Membr. Sci.* **2012**, *421−422*, 299−310.

(13) Yampolskii, Y. Polymeric Gas Separation Membranes. *Macromolecules* **2012**, *45*, 3298−3311.

(14) Jiao, Y.; Du, A.; Hankel, M.; Smith, S. C. Modelling carbon membranes for gas and isotope separation. *Phys. Chem. Chem. Phys.* **2013**, *15*, 4832.

(15) Yuan, W.; Chen, J.; Shi, G. Nanoporous graphene materials. *Mater. Today* **2014**, *17*, 77−85.

(16) Zhao, Y.; Xie, Y.; Liu, Z.; Wang, X.; Chai, Y.; Yan, F. Two-Dimensional Material Membranes: An Emerging Platform for Controllable Mass Transport Applications. *Small* **2014**, *10*, 4521−4542.

(17) Gadipelli, S.; Guo, Z. X. Graphene-based materials: Synthesis and gas sorption storage and separation. *Prog. Mater. Sci.* **2015**, *69*, 1−60.

(18) Fatemi, S. M.; Abbasi, Z.; Rajabzadeh, H.; Hashemizadeh, S. A.; Deldar, A. N. A review of recent advances in molecular simulation of graphene-derived membranes for gas separation. *Eur. Phys. J. D* **2017**, *71*, 194.

(19) Bunch, J. S.; Verbridge, S. S.; Alden, J. S.; van der Zande, A. M.; Parpia, J. M.; Craighead, H. G.; McEuen, P. L. Impermeable Atomic Membranes from Graphene Sheets. *Nano Lett.* **2008**, *8*, 2458−2462.

(20) Leenaerts, O.; Partoens, B.; Peeters, F. M. Graphene: A perfect nanoballoon. *Appl. Phys. Lett.* **2008**, *93*, 193107.

(21) Berry, V. Impermeability of graphene and its applications. *Carbon* **2013**, *62*, 1−10.

(22) en Jiang, D.; Cooper, V. R.; Dai, S. Porous Graphene as the Ultimate Membrane for Gas Separation. *Nano Lett.* **2009**, *9*, 4019−4024.

(23) Koenig, S. P.; Wang, L.; Pellegrino, J.; Bunch, J. S. Selective molecular sieving through porous graphene. *Nat. Nanotechnol.* **2012**, *7*, 728−732.

(24) Xie, G.; Yang, R.; Chen, P.; Zhang, J.; Tian, X.; Wu, S.; Zhao, J.; Cheng, M.; Yang, W.; Wang, D.; He, C.; Bai, X.; Shi, D.; Zhang, G. A General Route Towards Defect and Pore Engineering in Graphene. *Small* **2014**, *10*, 2280−2284.

(25) Zhou, D.; Cui, Y.; Xiao, P.-W.; Jiang, M.-Y.; Han, B.-H. A general and scalable synthesis approach to porous graphene. *Nat. Commun.* **2014**, *5*, 4716.

(26) Ohba, T. The Thinnest Molecular Separation Sheet by Graphene Gates of Single-Walled Carbon Nanohorns. *ACS Nano* **2014**, *8*, 11313−11319.

(27) Boutilier, M. S. H.; Sun, C.; O'Hern, S. C.; Au, H.; Hadjiconstantinou, N. G.; Karnik, R. Implications of Permeation through Intrinsic Defects in Graphene on the Design of Defect-Tolerant Membranes for Gas Separation. *ACS Nano* **2014**, *8*, 841−849.

(28) Jiao, Y.; Du, A.; Hankel, M.; Zhu, Z.; Rudolph, V.; Smith, S. C. Graphdiyne: a versatile nanomaterial for electronics and hydrogen purification. *Chem. Commun.* **2011**, *47*, 11843.

(29) Bartolomei, M.; Carmona-Novillo, E.; Hernández, M. I.; Campos-Martínez, J.; Pirani, F.; Giorgi, G. Graphdiyne Pores: "Ad Hoc" Openings for Helium Separation Applications. *J. Phys. Chem. C* **2014**, *118*, 29966−29972.
(30) Li, Y.; Zhou, Z.; Shen, P.; Chen, Z. Two-dimensional polyphenylene: experimentally available porous graphene as a hydrogen purification membrane. *Chem. Commun.* **2010**, *46*, 3672.
(31) Schrier, J. Helium Separation Using Porous Graphene Membranes. *J. Phys. Chem. Lett.* **2010**, *1*, 2284−2287.
(32) Blankenburg, S.; Bieri, M.; Fasel, R.; Müllen, K.; Pignedoli, C. A.; Passerone, D. Porous Graphene as an Atmospheric Nanofilter. *Small* **2010**, *6*, 2266−2271.
(33) Schrier, J. Carbon Dioxide Separation with a Two-Dimensional Polymer Membrane. *ACS Appl. Mater. Interfaces* **2012**, *4*, 3745−3752.
(34) Brockway, A. M.; Schrier, J. Noble Gas Separation using PG-ES X (X = 1 2, 3) Nanoporous Two-Dimensional Polymers. *J. Phys. Chem. C* **2013**, *117*, 393−402.
(35) Solvik, K.; Weaver, J. A.; Brockway, A. M.; Schrier, J. Entropy-Driven Molecular Separations in 2D-Nanoporous Materials with Application to High-Performance Paraffin/Olefin Membrane Separations. *J. Phys. Chem. C* **2013**, *117*, 17050−17057.
(36) Hu, W.; Wu, X.; Li, Z.; Yang, J. Helium separation via porous silicene based ultimate membrane. *Nanoscale* **2013**, *5*, 9062.
(37) Perim, E.; Paupitz, R.; Autreto, P. A. S.; Galvao, D. S. Inorganic Graphenylene: A Porous Two-Dimensional Material With Tunable Band Gap. *J. Phys. Chem. C* **2014**, *118*, 23670−23674.
(38) Li, F.; Qu, Y.; Zhao, M. Efficient helium separation of graphitic carbon nitride membrane. *Carbon* **2015**, *95*, 51−57.
(39) Peng, Y.; Li, Y.; Ban, Y.; Jin, H.; Jiao, W.; Liu, X.; Yang, W. Metal-organic framework nanosheets as building blocks for molecular sieving membranes. *Science* **2014**, *346*, 1356−1359.
(40) Schrier, J.; McClain, J. Thermally-driven isotope separation across nanoporous graphene. *Chem. Phys. Lett.* **2012**, *521*, 118−124.
(41) Hauser, A. W.; Schwerdtfeger, P. Nanoporous Graphene Membranes for Efficient 3 He/ 4 He Separation. *J. Phys. Chem. Lett.* **2012**, *3*, 209−213.
(42) Hauser, A. W.; Schrier, J.; Schwerdtfeger, P. Helium Tunneling through Nitrogen-Functionalized Graphene Pores: Pressure- and Temperature-Driven Approaches to Isotope Separation. *J. Phys. Chem. C* **2012**, *116*, 10819−10827.
(43) Mandrà, S.; Schrier, J.; Ceotto, M. Helium Isotope Enrichment by Resonant Tunneling through Nanoporous Graphene Bilayers. *J. Phys. Chem. A* **2014**, *118*, 6457−6465.
(44) Du, H.; Li, J.; Zhang, J.; Su, G.; Li, X.; Zhao, Y. Separation of Hydrogen and Nitrogen Gases with Porous Graphene Membrane. *J. Phys. Chem. C* **2011**, *115*, 23261−23266.
(45) Drahushuk, L. W.; Strano, M. S. Mechanisms of Gas Permeation through Single Layer Graphene Membranes. *Langmuir* **2012**, *28*, 16671−16678.
(46) Shaikhutdinov, S.; Freund, H.-J. Ultrathin Silica Films on Metals: The Long and Winding Road to Understanding the Atomic Structure. *Adv. Mater.* **2013**, *25*, 49−67.
(47) Weissenrieder, J.; Kaya, S.; Lu, J.-L.; Gao, H.-J.; Shaikhutdinov, S.; Freund, H.-J.; Sierka, M.; Todorova, T.; Sauer, J. Atomic Structure of a Thin Silica Film on a Mo(112) Substrate: A Two-Dimensional Network of SiO_4 Tetrahedra. *Phys. Rev. Lett.* **2005**, *95*, 076103.
(48) Löffler, D.; Uhlrich, J. J.; Baron, M.; Yang, B.; Yu, X.; Lichtenstein, L.; Heinke, L.; Büchner, C.; Heyde, M.; Shaikhutdinov, S.; Freund, H.-J.; Włodarczyk, R.; Sierka, M.; Sauer, J. Growth and Structure of Crystalline Silica Sheet on Ru(0001). *Phys. Rev. Lett.* **2010**, *105*, 146104.
(49) Yu, X.; Yang, B.; Boscoboinik, J. A.; Shaikhutdinov, S.; Freund, H.-J. Support effects on the atomic structure of ultrathin silica films on metals. *Appl. Phys. Lett.* **2012**, *100*, 151608.
(50) Yang, B.; Kaden, W. E.; Yu, X.; Boscoboinik, J. A.; Martynova, Y.; Lichtenstein, L.; Heyde, M.; Sterrer, M.; Włodarczyk, R.; Sierka, M.; Sauer, J.; Shaikhutdinov, S.; Freund, H.-J. Thin silica films on Ru(0001): monolayer bilayer and three-dimensional networks of [SiO4] tetrahedra. *Phys. Chem. Chem. Phys.* **2012**, *14*, 11344.
(51) Büchner, C.; Wang, Z.-J.; Burson, K. M.; Willinger, M.-G.; Heyde, M.; Schlögel, R.; Freund, H.-J. A Large-Area Transferable Wide Band Gap 2D Silicon Dioxide Layer. *ACS Nano* **2016**, *10*, 7982−7989.
(52) Büchner, C. Adding a Novel Material to the 2D Toolbox: Properties and Transfer of a Silica Bilayer. Ph.D. Thesis, Humboldt-Universität zu Berlin, 2016.
(53) Heyde, M.; Shaikhutdinov, S.; Freund, H.-J. Two-dimensional silica: Crystalline and vitreous. *Chem. Phys. Lett.* **2012**, *550*, 1−7.
(54) Lichtenstein, L.; Heyde, M.; Freund, H.-J. Atomic Arrangement in Two-Dimensional Silica: From Crystalline to Vitreous Structures. *J. Phys. Chem. C* **2012**, *116*, 20426−20432.
(55) Lichtenstein, L.; Heyde, M.; Freund, H.-J. Crystalline-Vitreous Interface in Two Dimensional Silica. *Phys. Rev. Lett.* **2012**, *109*, 106101.
(56) Emmez, E.; Yang, B.; Shaikhutdinov, S.; Freund, H.-J. Permeation of a Single-Layer SiO 2 Membrane and Chemistry in Confined Space. *J. Phys. Chem. C* **2014**, *118*, 29034−29042.
(57) Büchner, C.; Lichtenstein, L.; Stuckenholz, S.; Heyde, M.; Ringleb, F.; Sterrer, M.; Kaden, W. E.; Giordano, L.; Pacchioni, G.; Freund, H.-J. Adsorption of Au and Pd on Ruthenium-Supported Bilayer Silica. *J. Phys. Chem. C* **2014**, *118*, 20959−20969.
(58) Schlexer, P.; Giordano, L.; Pacchioni, G. Adsorption of Li Na, K, and Mg Atoms on Amorphous and Crystalline Silica Bilayers on Ru(0001): A DFT Study. *J. Phys. Chem. C* **2014**, *118*, 15884−15891.
(59) Schlexer, P.; Gianfranco Pacchioni, R. W.; Sauer, J. CO Adsorption on a Silica Bilayer Supported on Ru(0001). *Surf. Sci.* **2016**, *648*, 2−9.
(60) Kostinski, S.; Pandey, R.; Gowtham, S.; Pernisz, U.; Kostinski, A. Diffusion of Water Molecules in Amorphous Silica. *IEEE Electron Device Lett.* **2012**, *33*, 863−865.
(61) Blöchl, P. E. Projector augmented-wave method. *Phys. Rev. B: Condens. Matter Mater. Phys.* **1994**, *50*, 17953−17979.
(62) Kresse, G. From ultrasoft pseudopotentials to the projector augmented-wave method. *Phys. Rev. B: Condens. Matter Mater. Phys.* **1999**, *59*, 1758−1775.
(63) Perdew, J. P.; Burke, K.; Ernzerhof, M. Generalized Gradient Approximation Made Simple. *Phys. Rev. Lett.* **1996**, *77*, 3865−3868.
(64) Perdew, J. P.; Burke, K.; Ernzerhof, M. Erratum: Generalized Gradient Approximation Made Simple [Phys. Rev. Lett. 77 3865 (1996)]. *Phys. Rev. Lett.* **1997**, *78*, 1396−1396.
(65) Kresse, G.; Hafner, J. Ab initio molecular dynamics for liquid metals. *Phys. Rev. B: Condens. Matter Mater. Phys.* **1993**, *47*, 558−561.
(66) Kresse, G.; Hafner, J. Ab initio molecular-dynamics simulation of the liquid-metal−amorphous-semiconductor transition in germanium. *Phys. Rev. B: Condens. Matter Mater. Phys.* **1994**, *49*, 14251−14269.
(67) Kresse, G. Efficient iterative schemes for ab initio total-energy calculations using a plane-wave basis set. *Phys. Rev. B: Condens. Matter Mater. Phys.* **1996**, *54*, 11169−11186.
(68) Grimme, S. Semiempirical GGA-type density functional constructed with a long-range dispersion correction. *J. Comput. Chem.* **2006**, *27*, 1787−1799.
(69) Grimme, S.; Antony, J.; Ehrlich, S.; Krieg, H. A consistent and accurate ab initio parametrization of density functional dispersion correction (DFT-D) for the 94 elements H-Pu. *J. Chem. Phys.* **2010**, *132*, 154104.
(70) *CRC Handbook of Chemistry and Physics*, 96th ed.; Haynes, W., Ed.; CRC Press: Boca Raton, FL, 2015.
(71) Vrabec, J.; Stoll, J.; Hasse, H. A set of molecular models for symmetric quadrupolar fluids. *J. Phys. Chem. B* **2001**, *105*, 12126−12133.
(72) Stoll, J.; Vrabec, J.; Hasse, H. A set of molecular models for carbon monoxide and halogenated hydrocarbons. *J. Chem. Phys.* **2003**, *119*, 11396−11407.
(73) Harris, J. G.; Yung, K. H. Carbon dioxide's liquid-vapor coexistence curve and critical properties as predicted by a simple molecular model. *J. Phys. Chem.* **1995**, *99*, 12021−12024.
(74) Lichtenstein, L.; Büchner, C.; Yang, B.; Shaikhutdinov, S.; Heyde, M.; Sierka, M.; Włodarczyk, R.; Sauer, J.; Freund, H.-J. The

DOI: 10.1021/acsami.7b13302
ACS Appl. Mater. Interfaces 2017, 9, 43061−43071

Atomic Structure of a Metal-Supported Vitreous Thin Silica Film. *Angew. Chem., Int. Ed.* **2012**, *51*, 404−407.
(75) Mandrà, S.; Valleau, S.; Ceotto, M. Deep Nuclear Resonant Tunneling Thermal Rate Constant Calculations. *Int. J. Quantum Chem.* **2013**, *113*, 1722−1734.
(76) Kozuch, S.; Shaik, S. How to Conceptualize Catalytic Cycles? The Energetic Span Model. *Acc. Chem. Res.* **2011**, *44*, 101−110.
(77) Wang, Y.; Li, J.; Yang, Q.; Zhong, C. Two-Dimensional Covalent Triazine Framework Membrane for Helium Separation and Hydrogen Purification. *ACS Appl. Mater. Interfaces* **2016**, *8*, 8694−8701.
(78) Singh, A.; Koros, W. J. Significance of Entropic Selectivity for Advanced Gas Separation Membranes. *Ind. Eng. Chem. Res.* **1996**, *35*, 1231−1234.
(79) Oyama, S.; Lee, D.; Hacarlioglu, P.; Saraf, R. F. Theory of hydrogen permeability in nonporous silica membranes. *J. Membr. Sci.* **2004**, *244*, 45−53.
(80) Büchner, C.; Liu, L.; Stuckenholz, S.; Burson, K. M.; Lichtenstein, L.; Heyde, M.; Gao, H.-J.; Freund, H.-J. Building block analysis of 2D amorphous networks reveals medium range correlation. *J. Non-Cryst. Solids* **2016**, *435*, 40−47.
(81) Peters, T. A.; Fontalvo, J.; Vorstman, M. A. G.; Benes, N. E.; van Dam, R. A.; Vroon, Z. A. E. P.; van Soerst Vercammen, E. L. J.; Keurentjes, J. T. F. Hollow fibre microporous silica membranes for gas separation and pervaporation: Synthesis, performance and stability. *J. Membr. Sci.* **2005**, *248*, 73−80.

DOI: 10.1021/acsami.7b13302
ACS Appl. Mater. Interfaces 2017, 9, 43061−43071